greater than the viscosity of the convecting upper mantle by only one, or at most two, orders of magnitude [for example, (27)], suggesting that the continental lithosphere of Asia is more properly regarded as belonging to the fluid portion of the solid earth than to the relatively small fraction of Earth that behaves as rigid plates.

REFERENCES AND NOTES

1. W. Morgan, *J. Geophys. Res.* **73**, 1959 (1968); D. McKenzie and R. Parker, *Nature* **216**, 1276 (1967); C. DeMets, R. G. Gordon, D. F. Argus, S. Stein, *Geophys. J. Int.* **101**, 425 (1990); B. Isacks, J. Oliver, L. Sykes, *J. Geophys. Res.* **73**, 5855 (1968).
2. P. Molnar and P. Tapponnier, *Science* **189**, 419 (1975); P. Tapponnier and P. Molnar, *Nature* **264**, 319 (1976).
3. P. Bird and K. Piper, *Phys. Earth Planet. Inter.* **21**, 158 (1980); P. England and D. McKenzie, *Geophys. J. R. Astron. Soc.* **70**, 295 (1982); P. England, G. Houseman, L. Sonder, *J. Geophys. Res.* **90**, 3551 (1985); J. Vilotte, M. Daignières, R. Madariaga, *ibid.* **87**, 10709 (1982); J. Vilotte, R. Madariaga, M. Daignières, O. Zienkiewicz, *Geophys. J. R. Astron. Soc.* **84**, 279 (1986).
4. P. England and D. McKenzie, *Geophys. J. R. Astron. Soc.* **73**, 523 (1983).
5. We used a left-handed coordinate system, in which x is east, y is north, and z is down. The engineering convention for stresses was used, in which compressional stresses are negative [for example, L. Malvern, *Introduction to the Mechanics of a Continuous Medium* (Prentice-Hall, Englewood Cliffs, NJ, 1969)].
6. We recognize the abundant evidence for rheological layering in the lithosphere and the theoretical arguments [for example, P. Bird, *J. Geophys. Res.* **96**, 10275 (1991); L. H. Royden et al., *Science* **276**, 788 (1997)] that such layering may play an important role in deformation of Tibet. Because, however, the measurement of subsurface kinematics, let alone dynamics, is impossible, we confined our analysis to a simple structure.
7. G. Houseman and P. England, *J. Geophys. Res.* **91**, 3651 (1986).
8. The development follows that of (4) and (10), to which readers are referred for details.
9. The deviatoric stress tensor, τ, is defined by $\tau_{ij} = \sigma_{ij} - (1/3)\sigma_{kk}$ with the convention of summation over repeated subscripts. $(1/3)\sigma_{kk}$ (the negative of the pressure) is generally unimportant in the rheology of rocks of the lithosphere.
10. P. England and J. Jackson, *Annu. Rev. Earth Planet. Sci.* **17**, 197 (1989).
11. P. Molnar and H. Lyon-Caen, *Geol. Soc. Am. Spec. Pap.* **218**, 179 (1988); P. Molnar, P. England, J. Martinod, *Rev. Geophys.* **31**, 357 (1993).
12. We neglected basal tractions, though they may be incorporated in an analysis if an adequate method is available for specifying such tractions from observations [S. Wdowinski, R. O'Connell, P. England, *J. Geophys. Res.* **94**, 10331 (1989); S. Ellis, P. Fullsack, C. Beaumont, *Geophys. J. Int.* **120**, 24 (1995)].
13. L. Sonder and P. England [*Earth Planet. Sci. Lett.* **77**, 81 (1986)] show that Eq. 5 represents the vertical average, throughout the lithosphere, of several mechanisms, including frictional slip on faults in the upper 10 to 20 km of the crust and power-law creep with $n \sim 3$ in the deeper levels of the lithosphere, where ductile deformation occurs [J. Weertman, *Rev. Geophys. Space Phys.* **8**, 145 (1970)]. No unambiguous physical significance can be assigned to n in Eq. 5, but as a rule of thumb, n lies close to 3 where the strength of the lithosphere is dominated by its ductile layer and increases as the contribution to strength made by faults in the upper crust increases (13).
14. We calculated potential energies following the procedure of [(15), appendix], assuming that crust 35 km thick has a surface height of 250 m and that the lithosphere thickness is 100 km. The influence of varying these values, respectively, between 30 and 45 km, and between 100 and 200 km, is to change the quantities derived in this paper (Figs. 3 and 4;
Table 1) by less than 50%.
15. P. England and G. Houseman, *J. Geophys. Res.* **94**, 17561 (1989).
16. C. Jones, J. Unruh, L. Sonder, *Nature* **381**, 37 (1996).
17. P. Molnar and Q. Deng, *J. Geophys. Res.* **89**, 6203 (1984); J. Jackson and D. McKenzie, *Geophys. J. Int.* **93**, 45 (1988); G. Ekström and P. England, *J. Geophys. Res.* **94**, 10231 (1989).
18. W. E. Holt, J. F. Ni, T. C. Wallace, A. J. Haines, *J. Geophys. Res.* **96**, 14595 (1991); W. E. Holt, M. Li, A. J. Haines, *Geophys. J. Int.* **122**, 569 (1995).
19. P. England and P. Molnar, *Geophys. J. Int.* **130**, 557 (1997).
20. G. Peltzer and F. Saucier, *J. Geophys. Res.* **101**, 27943 (1996).
21. A. J. Haines, *Geophys. J. R. Astron. Soc.* **68**, 203 (1982); _____ and W. E. Holt, *J. Geophys. Res.* **98**, 12057 (1993); J. Jackson, A. J. Haines, W. Holt, *ibid.* **97**, 17657 (1992); _____, *ibid.* **100**, 15205 (1995).
22. St. Venant's equations of strain compatibility derive from the definitions of strain rates as derivatives of the components of velocity, for example, Eq. 6. Thus, strain rates derived by differentiating the components of a velocity field are internally consistent throughout the region where the velocity field is known, whereas strain rates estimated piecemeal from faulting or earthquakes need not be consistent with each other [for example, (21)].
23. B. Kostrov, *Izv. Acad. Sci. USSR Phys. Solid Earth* **97**, 23 (1974).
24. To appreciate the influence of variations of B on estimates of potential energy, consider a one-dimensional rendition of Eq. 3: $L\partial\bar{\tau}_{xx}/\partial x = \partial\Gamma/\partial x$. With variation in B and approximation of derivatives by differences over a unit length, we can write: $LB\Delta\dot{\varepsilon}_{xx}^{1/n} + L\dot{\varepsilon}_{xx}^{1/n}\Delta B \approx \Delta\Gamma$. For $L = 100$ km, $\dot{\varepsilon}_{xx} = 10^{-15}$ s^{-1}, and $n = 3$, the potential energy associated with the neglected second term on the left-hand side of this equation is $\Delta\Gamma \approx \Delta B$. Therefore, neglecting ΔB of order B is equivalent to introducing a spurious potential energy of order B ($\approx 2 \times 10^{12}$ N m^{-1}; Fig. 4).
25. P. Molnar and P. Tapponnier, *Earth Planet. Sci. Lett.* **52**, 107 (1981); J. Vilotte, M. Daignières, R. Madariaga, O. Zienkiewicz, *Phys. Earth Planet. Inter.* **36**, 236 (1984); P. England and G. Houseman, *Nature* **315**, 297 (1985); E. A. Neil and G. A. Houseman, *Tectonics* **16**, 571 (1997).
26. N. A. Logatchev, Y. A. Zorin, V. A. Rogozhina, *Tectonophysics* **94**, 223 (1983); I. Baljinnyam et al., *Geol. Soc. Am. Mem.* **181**, (1993).
27. J. Mitrovica, *J. Geophys. Res.* **101**, 555 (1996); _____ and A. Forte, *ibid.* **102**, 2751 (1997).
28. Funded in part by the National Environment Research Council (U.K.) grant GR3/9183 to P.E., who is grateful for support from the Division of Geological and Planetary Sciences, California Institute of Technology, while part of this work was carried out. Also supported by NSF under grant EAR9527024 to P.M. Figures were produced with GMT [P. Wessel and W. H. F. Smith, *Eos* **76**, 329 (1995)], and the text was prepared with GNUemacs.

29 May 1997; accepted 12 September 1997

Deformation in the Lower Crust of the San Andreas Fault System in Northern California

Timothy J. Henstock, Alan Levander, John A. Hole

A continuous seismic velocity and reflectivity cross-section of the San Andreas fault system in northern California shows offsets in the lower crust and the Mohorovičić Discontinuity near the San Andreas and Maacama strike-slip faults. These faults may cut through the crust to the upper mantle in a zone less than 10 kilometers wide. The northern California continental margin to the eastern edge of the Coast Ranges is underlain by a high-velocity lowermost crustal layer that may have been emplaced within 2 million years following the removal of the Gorda plate slab. The rapid emplacement and structure within this layer are difficult to reconcile with existing tectonic models.

The relation between deformation in the crust and mantle is uncertain. A key area in which to examine this relation is the San Andreas fault fault system (SAFS) in northern California. Here, the SAFS includes the San Andreas fault (SAF), Maacama fault (MF), and Bartlett Springs fault (BSF). We wish to know whether the faults cut directly through the crust and into the mantle, or whether the upper crustal faults are linked by sub-horizontal detachments to the lower crust and mantle, so that motion in the mantle is not directly coupled to that in the overlying crust. The development of the SAFS is related to the migration of the Mendocino Triple Junction (MTJ) (1). As the MTJ migrated northward, the Gorda

T. J. Henstock and A. Levander, Department of Geology and Geophysics, MS-126, Rice University, Houston, TX 77005–1892, USA.
J. A. Hole, Department of Geological Sciences, Virginia Polytechnic Institute, Blacksburg, VA 24061–0420, USA.

slab is thought to have been removed from beneath northern California and replaced by the upwelling of asthenospheric mantle (2).

Here, we present results from the 1993 and 1994 MTJ seismic experiments (3, 4) along an east-west line at latitude 39.4°N extending from the Pacific Ocean basin to the eastern side of the Coast Ranges (Fig. 1A). Gravity (5), teleseismic (6), and crustal seismic data (4) suggest that the southern edge of the Gorda slab lies 50 to 100 km to the north of the profile. Recent volcanism, dated at 2 Ma, in the Clear Lake region 50 to 100 km to the south of the profile has been attributed to upwelling in the wake of MTJ migration (7).

We developed a P-wave seismic velocity model using the travel times (8) of reflected and refracted arrivals from land, marine, and onshore-offshore recordings (Fig. 1C). The seismic velocity model shows that the upper-
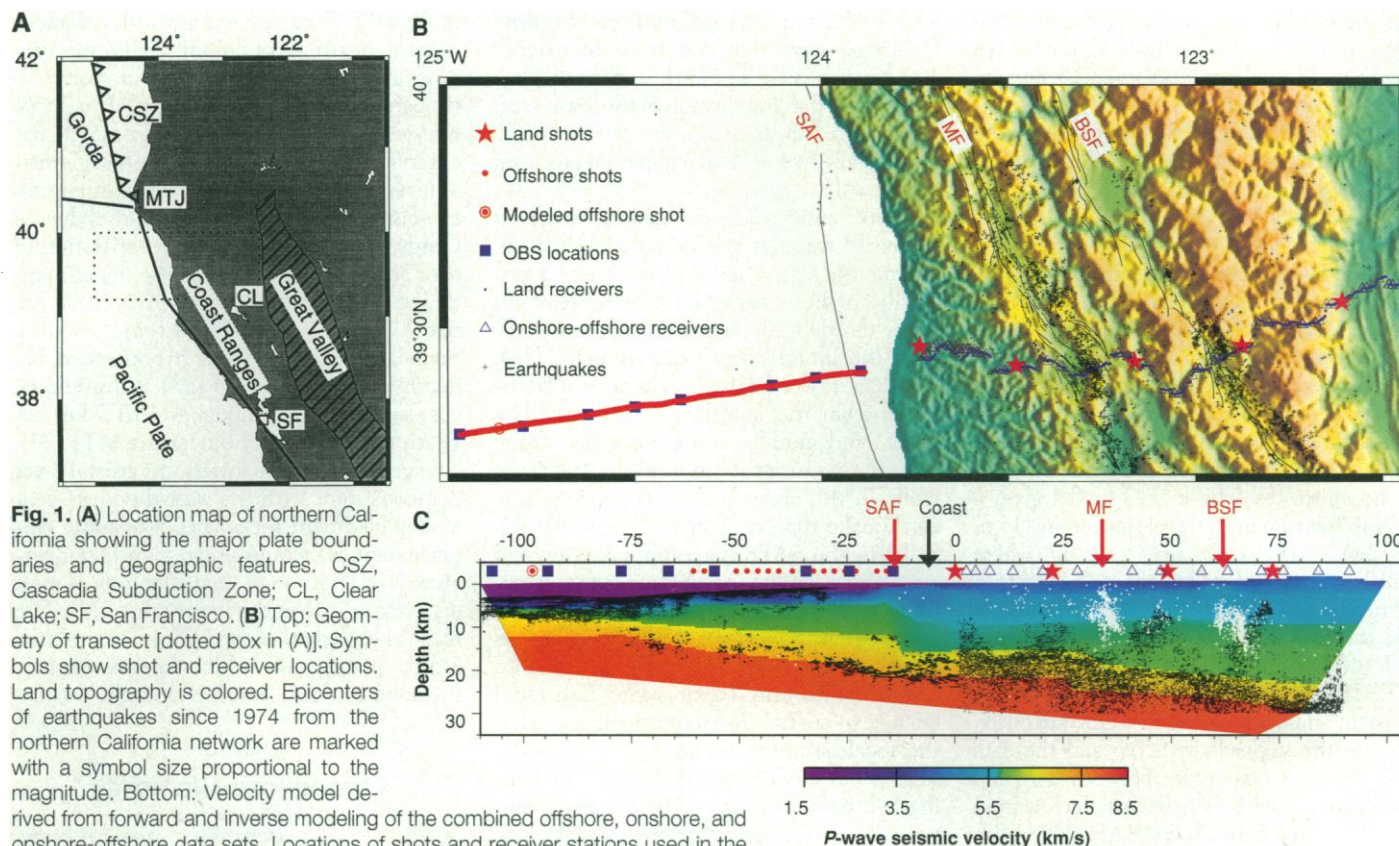
Fig. 1. (A) Location map of northern California showing the major plate boundaries and geographic features. CSZ, Cascadia Subduction Zone; CL, Clear Lake; SF, San Francisco. **(B)** Top: Geometry of transect [dotted box in (A)]. Symbols show shot and receiver locations. Land topography is colored. Epicenters of earthquakes since 1974 from the northern California network are marked with a symbol size proportional to the magnitude. Bottom: Velocity model derived from forward and inverse modeling of the combined offshore, onshore, and onshore-offshore data sets. Locations of shots and receiver stations used in the modeling are shown. Earthquake hypocenters projected onto the section are plotted in white. A continuous, depth-migrated reflection section (*13*) is overlain in black.

most crust (about 0 to 5 km depth) contains low-velocity basins that are up to 4 km deep offshore but generally less than 2 km deep onshore. Beneath the basins, velocities increase gradually from 5 km/s to 5.9 km/s at the base of the apparently simple accretionary complex (*9*). The lowermost crustal layer (LCL) (about 9 to 15 km depth) is 5 to 6 km thick and has velocities up to 7.2 to 7.3 km/s. The LCL is offset vertically at its top and bottom at −20 to −25 km west and

25 to 30 km east of the center point (0 km) of the transect. The east and west offsets lie below and to the west of the surface traces of the MF and SAF (Fig. 1C), respectively. Onshore, the lowermost crust coincides with a series of bright reflections that are also offset vertically at the MF. The structure of the lowermost crust is determined primarily from the travel times of the upper mantle refracted primary wave P_n and the Mohorovičić Discontinuity (Moho) reflection

P_mP in the onshore-offshore data, and from near-vertical reflections onshore and offshore. The combination of near-vertical and wide-angle data improves the resolution of the model by providing greater spatial and angular distribution of the ray paths (*10*).

We generated finite-difference synthetic seismograms for a shot near $X = -98$ km (Fig. 1B), to compare with the P_n waves recorded by the onshore receivers (Fig. 2). The simple near-source structure means that energy en-
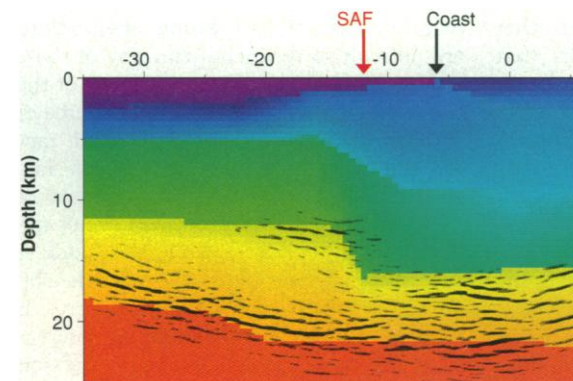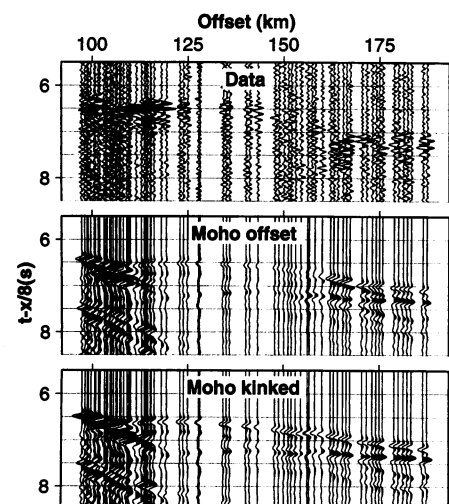

Fig. 2 (left). Top: Upper mantle refraction P_n (the first arrival) recorded at the onshore-offshore receivers. Ten shots near $X = -98$ km were stacked to enhance energy with an apparent velocity of 8 km/s. Statics have been applied to account for elevation differences. Synthetic seismograms were generated for two velocity models. Middle: Stepped model with a Moho offset beneath the SAF and MF. Bottom: Kinked model with a Moho that is kinked at the SAF. The kinked model shows mismatches in the travel time and relative amplitude of the P_n arrival. On each panel an arrival with an apparent velocity of 8 km/s is horizontal. **Fig. 3 (right).** Depth migrated onshore-offshore reflectivity data of the crust near the SAF, superimposed onto the velocity model. We interpret the deeper high-amplitude reflectors as the Moho. The subhorizontal reflector at 12 km depth in the west and 16 km depth in the east represents the top of the LCL.

ters the mantle along similar paths, so differences in the recorded arrivals arise near the receivers. This allowed us to sum 10 shots to improve signal strength. Two different velocity models were tested. One was equivalent to our final velocity model in which the Moho has steps beneath the SAF and MF ("stepped"). The other had the same Moho depths at the base of the continental slope, immediately east of the SAF, and beneath the east side of the Coast Ranges ("kinked") (11). Some change in the slope of the Moho near the SAF is required to match the observed travel times. Both models included the same stepped structure at the top of the LCL, so that differences in the synthetic seismograms arise only from differences in the assumed Moho structures. The kinked model gives a smooth increase in P_n travel time, from 115 to 190 km offset, except near 160 km, where travel times are affected by the kink at the top of the LCL. In contrast, the stepped synthetic and the data show flat arrivals between 115 and 160 km and between 170 and 190 km (12). The kinked synthetics show a relatively constant amplitude from 115 to 180 km offset, whereas the stepped synthetics and the data show lowered amplitudes between 115 and 160 km offset due to a geometric shadow from the Moho step beneath the SAF.

We show the reflectivity data of the lower crust (Fig. 3) spanning the SAF made by prestack depth migration of wide-angle onshore-offshore data (13). The migration velocity field included all the near surface complexity, but at depth was smoother than the inverted velocities. No assumptions about the location of reflectors were imposed, giving an essentially independent check on the geometry of the lowermost crust and better resolution than travel-time modeling. The top of the LCL is offset 5 km beneath the SAF, whereas the Moho is offset 2 km over less than 5 km laterally, some 10 km west of the SAF. Immediately west of the SAF these offsets thicken the LCL to almost 10 km.

Seismicity near our profile is mostly shallower than 15 km (Fig. 1). Most other strike-slip faults or transform faults that have been studied do not show a relation between the strike-slip motion in the crust and the structure of the Moho, although this does not rule out the possibility that the crust and mantle are coupled beneath strike-slip faults.

We interpret the vertical offsets in velocity at the top and bottom of the LCL beneath the SAF and MF (Fig. 1C) as extensions of these strike-slip faults into the mantle. Our interpretation differs from tectonic interpretations of the San Francisco area that link the shallow strike-slip faults with a sub-horizontal detachment (14, 15), but is consistent with the model inferring vertical whole-crustal boundaries (16) for the data from the San Francisco

area. Reflection lines run offshore of central California show that oceanic crust extends 100 km beneath the North American plate and suggest that imbrication of the lower crust has occurred in discrete zones related to the Hosgri fault system (17), a potential precursor of the SAF.

Plate motions are assumed to be driven primarily through the convective flow in the mantle, but seismicity is observed primarily in the upper crust. Having strength reside mostly in the upper crust is consistent with the limited depth of seismicity (14), but does not explain how strain is transferred from the mantle to the crust. The lower and middle crust may be strong enough to transfer strain from the mantle to faults in the upper crust without requiring earthquake rupture. Some of the strike-slip faults in the SAFS have formed along and reactivated earlier subduction zone structures (18). Earthquakes north of the MTJ are broadly distributed, while earthquakes south of the MTJ are concentrated into narrow bands only 10 km wide. This rapid change in spatial distribution suggests that the localization of seismicity south of the MTJ is not due to extended strain-weakening, but perhaps is caused by the segmentation of mantle upwelling into a slab window, analogous to the segmentation of mid-ocean ridge systems. Offsets in lower crustal structure that are close to the loci of strike-slip motion are then a consequence of the northeast dip of the Moho (4).

A similar LCL with velocities appropriate for oceanic crust is seen in many places along the California margin south of the MTJ (16, 17, 19). This higher-velocity LCL may be: (i) Pacific plate oceanic crust overridden by the North American plate following the migration of the MTJ (19); (ii) Farallon plate crust captured by the Pacific plate (20); (iii) unsubducted Gorda plate fragments; (iv) ophiolitic rocks linked with the Great Valley basement rocks (21); or (v) igneous rocks solidified in situ from mantle melts (2). Our seismic observations are difficult to reconcile with any of these models because (a) the broad extent of the high-velocity LCL implies a large source or sources; (b) emplacement of the LCL rapidly follows the removal of the Gorda slab; (c) the LCL extends 100 km landward of the SAF and 160 km from the base of the continental slope offshore; (d) the LCL is flat to east-dipping but cut by strike-slip motion. Recently overridden Pacific crust is an unlikely mechanism because of observations (b) and (c), which require contraction across the SAFS at a rate equivalent to the SAF transform motion. The offsets in the LCL also make the large-scale transfer of material across the strike-slip faults implausible. Microplate capture requires transport

of the LCL along the margin with a detachment beneath all of coastal California slipping at up to the total SAF motion. Although contraction across the SAF at 5 to 6 mm/year (22) since 30 Ma can match the extent of the high-velocity lowermost crustal layer, such a detachment without recorded seismicity seems unlikely. Unsubducted Gorda plate crust requires the separation of the Gorda plate crust from the upper mantle, because the slab-window hypothesis explains many large-scale tectonic features. Such a process has been hypothesized beneath Vancouver Island (23) and would be consistent with earthquakes 4 to 5 km beneath the Gorda Moho near the MTJ (24). The geometry of the lowermost crustal layer is inconsistent with the west-dipping Great Valley basement rocks (iv). Magmatic emplacement (v) requires high mantle temperatures (25), although small amounts of melt are present within the lower crust (26). The most likely origin of the LCL is underplated Gorda plate crust, which is subsequently intruded by small volumes of melt.

REFERENCES AND NOTES

1. The MTJ is a complex region where the Pacific, Gorda, and North American plates have interacted since the Pacific–Farallon spreading center was subducted at 27 Ma [T. Atwater, *Geol. Soc. Am. Bull.* **81**, 3513 (1970).] North of the MTJ, Gorda plate lithosphere is subducted beneath the North American plate, while the Pacific–North American and Pacific–Gorda plate boundaries are zones of predominantly strike-slip motion (Fig. 1A). Global analyses [C. DeMets, R. G. Gordon, S. Stein, D. F. Argus, *Geophys. Res. Lett.* **14**, 911 (1987)] show the Pacific plate moving northward at 50 mm/year with respect to the North American plate, although detailed studies [D. F. Argus and R. G. Gordon, *Geology* **19**, 1085 (1991)] give a Pacific–Great Valley motion of only 40 mm/year. Rigid plate tectonics implies that the MTJ migrates with the Pacific plate.
2. K. P. Furlong, *Tectonophysics* **223**, 149 (1993).
3. A. M. Trehu and the Mendocino Working Group, *Eos* **76**, 369 (1995).
4. B. C. Beaudoin *et al.*, *Geology* **24**, 195 (1996).
5. R. C. Jachens and A. Griscom, *J. Geophys. Res.* **88**, 9375 (1983).
6. H. M. Benz, G. Zandt, G. D. H. Oppenheimer, *ibid.* **97**, 4791 (1992).
7. K. F. Fox, R. J. Fleck, G. H. Curtis, C. E. Meyer, *Geol. Soc. Am. Bull.* **96**, 647 (1985).
8. C. Zelt and R. B. Smith, *Geophys. J. Int.* **108**, 16 (1992). We modeled 6000 travel times from 43 shot and receiver locations including crustal refractions, reflections from the top of the LCL and the Moho (P_mP), and the upper mantle refraction (P_n). Marine reflection data constrained the structure of sedimentary basins offshore. Different models fitting the data show that absolute depths of the LCL interfaces are uncertain by about 2 km, with relative depths uncertain by 1 km. Most of the differences are east of $X = 60$ km and deeper than $Z = 15$ km, where angular coverage is incomplete. We tested models with simpler boundaries for the lowermost crustal layer, including flat upper and lower boundaries, the stepped upper (Fig. 1C) and flat lower boundaries, and the stepped upper (Fig. 1C) and a kinked lower boundary. None fit the lower crustal and upper mantle travel times, although all fit the upper crustal arrivals and have equal Moho depths

at X = −75 km and X = 90 km.

9. The heterogeneity within the Franciscan accretionary terranes [J. A. Goff and A. R. Levander, *J. Geophys. Res.* **101**, 8489 (1996)] is not resolved. Upper crustal velocities change (by 0.1 to 0.2 km/s) across the SAF, representing the difference between an old accretionary wedge and terranes involved in subduction until 2 to 3 Ma.

10. Apparent lower-crustal offsets in reflection data could be caused by basins near the fault zones or by changes in crustal velocities across the faults. However, to explain travel-time anomalies in wide-angle reflections and refractions by shallow structure would require basins offset from the faults, because these arrivals travel laterally through the crust. The simplest explanation for all the observations is that the anomalies arise near the base of the crust.

11. The kinked velocity model has a Moho slope of 10° west of the surface trace of the SAF and a Moho slope of 5° east of the SAF surface trace, so that the kink describes the point where the slope changes. The depths of the Moho at the endpoints of the slopes are: 12 km at X = −77 km, 21 km at X = −20 km, and 29 km at X = 80 km.

12. The rms travel-time misfit for 3100 lower crustal and upper mantle picks is 164 ms for the stepped model, with a reduced χ^2 of 1.4, compared with 186 ms and 1.9 for the kinked model. Most of the additional error arises in the onshore-offshore P_n phase.

13. Depth migration focuses reflected energy at the reflector location [W. A. Schneider, *Geophysics* **43**, 49, (1978)]. It is routinely applied to near-vertical data; our application to onshore-offshore data links marine reflection data and a single-fold land section. The different data types cause changes in appearance of the section at X = −30 km and X = 1 km on the profile.

14. K. P. Furlong, W. D. Hugo, G. Zandt, *J. Geophys. Res.* **94**, 3100 (1989).

15. T. M. Brocher *et al.*, *Science* **265**, 1436 (1994).

16. W. S. Holbrook, T. M. Brocher, U. S. ten Brink, J. A. Hole, *J. Geophys. Res.* **101**, 22311 (1996).

17. A. S. Meltzer and A. R. Levander, *ibid.* **96**, 6475 (1991); J. M. Howie, K. C. Miller, W. U. Savage, *ibid.* **98**, 8173 (1993); K. C. Miller, J. M. Howie, S. D. Ruppert, *ibid.* **97**, 19961 (1992); C. F. Lafond and A. Levander, *ibid.* **100**, 22231 (1995).

18. H. M. Kelsey and G. A. Carver, *ibid.* **93**, 4797 (1988); D. A. Castillo and W. L. Ellsworth, *ibid.* **98**, 6543 (1993).

19. B. M. Page and T. M. Brocher, *Geology* **21**, 635 (1993).

20. R. G. Bohannon and T. Parsons, *Geol. Soc. Am. Bull.* **107**, 937 (1995).

21. R. C. Jachens, A. Griscom, C. W. Roberts, *J. Geophys. Res.* **100**, 12769 (1995).

22. This is within the limits of DeMets *et al.* (1) but is higher than the 95% limits of −1 to +5 mm/year for present shortening of Argus and Gordon (1).

23. A. J. Calvert, *Can. Jour. Earth Sci.* **33**, 1294 (1996).

24. S. W. Smith, J. S. Knapp, R. C. McPherson, *J. Geophys. Res.* **98**, 8153 (1993).

25. Assumptions that adiabatic upwelling of mantle into the slab window extends to the base of the accretionary rocks and fills the space vacated by the Gorda slab allow us to use published calculations [D. McKenzie and M. J. Bickle, *J. Petrol.* **29**, 625 (1988)] to estimate the melt generated. For 1300°C mantle, this is about 2 km, and to explain the thickness of the LCL would require temperatures 100° to 150°C higher. Petrologic consequences of higher mantle temperatures are discussed by McKenzie and Bickle.

26. To match the wide-angle velocity structure and near-vertical reflectivity requires thin bodies with too great a material contrast for a solid-solid contact so that fluids must be present. Our interpretation that these represent melt intrusions is based on the tectonic setting [A. Levander *et al.*, in preparation].

27. We are grateful to the many people who assisted in the 1993 and 1994 field programs, the IRIS-PASSCAL program, and Lamont-Doherty Earth Observatory. Earthquake locations were obtained from the northern California earthquake network operated by the U.S. Geological Survey and the

Synthesis of Nanoparticles and Nanotubes with Well-Separated Layers of Boron Nitride and Carbon

K. Suenaga, C. Colliex,* N. Demoncy, A. Loiseau, H. Pascard, F. Willaime

Polyhedral and tubular graphitic nanoparticles made of carbon layers and boron nitride (BN) layers have been synthesized. These particles were observed in the soot collected on the anode deposit formed by arcing a hafnium diboride rod with graphite in a nitrogen atmosphere. Elemental profiles with subnanometer-scale resolution revealed a strong phase separation between BN layers and carbon layers along the radial direction. Most of these tubes have a sandwich structure with carbon layers both in the center and at the periphery, separated by a few BN layers. This structure provides insight into the atomistic mechanism of nanotube growth in the boron-carbon-nitrogen ternary system and may lead to the creation of nanostructured electronic devices relying on the controlled production of heteroatomic nanotubes.

The family of graphitic nanoparticles with tubular or spherical shape has expanded rapidly since the discovery of carbon nanotubes (1) and carbon onions (2), which consist of a few concentric cylindrical or spherical carbon layers. Their pure BN analogs have now been successfully synthesized (3–5). The electronic properties of these nanoparticles open up new possibilities for making nanoscale electronic devices, in particular from the tubular form (6). On the basis of theoretical predictions suggesting that the electronic properties of carbon nanotubes will range from metallic to semiconducting with a small gap, depending on the tube diameter and chirality (7), the idea of making electronic switches by connecting pure carbon nanotubes was first proposed (8). This concept was recently generalized to heterojunctions between

K. Suenaga, Laboratoire de Physique des Solides, URA 002, Université de Paris-Sud, Bât. 510, 91405 Orsay, France.
C. Colliex, Laboratoire de Physique des Solides, URA 002, Université de Paris-Sud, Bât. 510, 91405 Orsay, France, and Laboratoire Aimé Cotton, UPR 3321, Campus d'Orsay, Bât. 505, 91405 Orsay, France.
N. Demoncy, Laboratoire des Solides Irradiés, CEA-CNRS, Ecole Polytechnique, 91128 Palaiseau Cédex, France, and Laboratoire de Physique des Solides, Office National d'Etudes et de Récherches Aérospatiales, BP 72, 92322 Châtillon, France.
A. Loiseau, Laboratoire de Physique des Solides, Office National d'Etudes et de Recherches Aérospatiales, BP 72, 92322 Châtillon, France.
H. Pascard, Laboratoire des Solides Irradiés, CEA-CNRS, Ecole Polytechnique, 91128 Palaiseau, France.
F. Willaime, Section de Recherches de Métallurgie Physique, CEA/Saclay, 91191 Gif-sur-Yvette, France.

*To whom correspondence should be addressed.

$B_xC_yN_z$ nanotubes with different chemical compositions (9). The advantage of such nanotubes is that their electronic properties are primarily determined by composition and are thus relatively easy to control. For example, BN nanotubes are predicted to be semiconducting, with a wide gap close to the 5.8-eV gap of bulk hexagonal BN (10). In this context, uniformly doped carbon nanotubes, as well as nanotubes with other chemical compositions such as BC_2N or BC_3 (11), would be interesting for their electronic properties. However, their synthesis has not yet been achieved in a controllable fashion, although portions of such tubes among a majority of pure carbon tubes have been reported (12–14).

Here, we report the synthesis of a soot containing polyhedral and tubular nanoparticles that consist of well-separated BN layers and carbon layers. In previous arc-discharge syntheses of B-C-N tubes, it was shown that when the anode contains carbon, the graphitic products contain mostly carbon (12–14). Either a low doping by B and N (less than 2%) or very low concentrations of B-rich or BN-rich nanotubes have been reported. In our study, this drawback was overcome by modifying the original geometry used to produce pure BN tubes (5). A graphite cathode—used instead of the original HfB_2 rod—is arced with an HfB_2 anode in a nitrogen atmosphere. In the present configuration, the three constituents have different sources: the anode for boron, the cathode (which slightly vaporizes in the present case) for carbon, and the